



# Can the Local Bubble explain the radio background?

Martin G. H. Krause   and Martin J. Hardcastle 

*Centre for Astrophysics Research, School of Physics, Astronomy and Mathematics, University of Hertfordshire, College Lane, Hatfield, Hertfordshire AL10 9AB, UK*

Accepted 2021 January 9. Received 2021 January 9; in original form 2020 October 9

## ABSTRACT

The ARCADE 2 balloon bolometer along with a number of other instruments have detected what appears to be a radio synchrotron background at frequencies below about 3 GHz. Neither extragalactic radio sources nor diffuse Galactic emission can currently account for this finding. We use the locally measured cosmic ray electron population, demodulated for effects of the Solar wind, and other observational constraints combined with a turbulent magnetic field model to predict the radio synchrotron emission for the Local Bubble. We find that the spectral index of the modelled radio emission is roughly consistent with the radio background. Our model can approximately reproduce the observed antenna temperatures for a mean magnetic field strength  $B$  between 3 and 5 nT. We argue that this would not violate observational constraints from pulsar measurements. However, the curvature in the predicted spectrum would mean that other, so far unknown sources would have to contribute below 100 MHz. Also, the magnetic energy density would then dominate over thermal and cosmic ray electron energy density, likely causing an inverse magnetic cascade with large variations of the radio emission in different sky directions as well as high polarization. We argue that this disagrees with several observations and thus that the magnetic field is probably much lower, quite possibly limited by equipartition with the energy density in relativistic or thermal particles ( $B = 0.2\text{--}0.6$  nT). In the latter case, we predict a contribution of the Local Bubble to the unexplained radio background at most at the per cent level.

**Key words:** ISM: bubbles – local interstellar matter – diffuse radiation – radio continuum: general – radio continuum: ISM.

## 1 INTRODUCTION

The balloon-borne precision bolometer ARCADE 2 has reported an excess emission above the cosmic microwave background (CMB) of  $54 \pm 6$  mK at 3 GHz (Fixsen et al. 2011). Together with measurements from the Long Wavelength Array at 40–80 MHz and other measurements (Dowell & Taylor 2018), this forms the extragalactic radio background, which dominates the sky emission below 1 GHz. When the contributions from the CMB and the Milky Way are removed, an isotropic component with a power-law spectrum with index  $-2.58$  when plotting antenna temperature versus frequency remains ( $\alpha = 0.58$  for flux density  $S \propto \nu^{-\alpha}$ ). The relevant frequency range includes the 60–80 MHz region, where the 21-cm signal from the epoch of reionization is expected. An absorption feature of less than 1 per cent of the radio background emission has indeed been found by the Experiment to Detect the Global Epoch of Reionization Signature (EDGES) at these frequencies (Bowman et al. 2018). For the interpretation of the absorption feature as of cosmological origin, it is important to understand whether the radio synchrotron background is produced locally or at high redshift (e.g. Monsalve et al. 2019; Ewall-Wice, Chang & Lazio 2020).

Since the contribution from the Milky Way has a distinct geometry and is accounted for already in the aforementioned results, the most straightforward explanation would be a large population of known extragalactic radio sources, namely radio loud active galactic nuclei

and star-forming galaxies. At 3 GHz, measurements with the Karl G. Jansky Very Large Array find a combined antenna temperature for all such sources of 13 mK, significantly below the ARCADE 2 result (Condon et al. 2012). A similar measurement has recently been performed with the Low-Frequency Array (LOFAR) with the similar result that only about 25 per cent of the radio background can be accounted for by resolved radio sources (Hardcastle et al. 2020). Another suggestion that has been put forward is a Galactic halo of cosmic ray electrons with a scale length of 10 kpc (Orlando & Strong 2013; Subrahmanyan & Cowsik 2013). The required particle population would however also produce X-rays via inverse Compton scattering, which would violate observational constraints (Singal et al. 2010). Also, such a prominent radio halo would be atypical for galaxies like the Milky Way (Singal et al. 2015; Stein et al. 2020), even though haloes of up to a few kpc at 150 MHz have been found recently (Stein et al. 2019). These difficulties have inspired a number of interesting explanations, including for example free-free emission related to galaxy formation at high redshift (Liu et al. 2019) and dark matter annihilation (Hooper et al. 2012). See Singal et al. (2018) for a recent review.

We investigate here a comparatively simple explanation: synchrotron emission from the Local Bubble. The Local Bubble is a low-density cavity in the interstellar medium around the Solar system (e.g. Cox & Reynolds 1987). The superbubble was likely formed by winds and explosions of massive stars (Breitschwerdt et al. 2016; Schulreich et al. 2018). Hot gas in the bubble contributes significantly to the soft X-ray background (Snowden et al. 1997, 1998; Galeazzi et al. 2014; Snowden 2015). The boundary is delineated by a dusty

\* E-mail: [m.g.h.krause@herts.ac.uk](mailto:m.g.h.krause@herts.ac.uk)

shell that has been mapped with absorption data against stars with known distances (Lallement et al. 2014; Snowden et al. 2015b; Pelgrims et al. 2020). Direct observation of the likely present neutral hydrogen supershell is difficult against the background of the Milky Way, but the distinct structure of erosion of the interface towards a neighbouring superbubble has been observed (Krause et al. 2018). Similar features are also known from NaI and HI absorption studies (Lallement et al. 2014). Interaction of cosmic ray particles with the supershell may explain the high-energy neutrinos observed with IceCube (Andersen, Kachelriess & Semikoz 2018; Bouyahiaoui, Kachelriess & Semikoz 2020). The superbubble contains high-ionization species (Breitschwerdt & de Avillez 2006), filaments and clouds of partially neutral and possibly even molecular gas (e.g. Gry & Jenkins 2014, 2017; Redfield & Linsky 2008, 2015; Snowden et al. 2015a; Farhang et al. 2019; Linsky, Redfield & Tilipman 2019) and is threaded by magnetic fields (e.g. Andersson & Potter 2006; McComas et al. 2011; Frisch et al. 2015; Alves et al. 2018; Pirola et al. 2020). It has already been suggested as the physical origin of high-latitude radio emission by Sun et al. (2008).

We first make an empirical model based on a comparison to the non-thermal superbubble in the dwarf galaxy IC 10 (Section 2) and then present a detailed model based on the locally observed population of cosmic ray electrons and available constraints on the magnetic field in the Local Bubble (Section 3). We discuss our findings in the context of the observational constraints in Section 4 and conclude in Section 5 that a dominant contribution of the Local Bubble to the radio background seems unlikely.

## 2 EMPIRICAL MODEL BY COMPARING TO THE NON-THERMAL SUPERBUBBLE IN IC 10

Superbubbles are not usually known to emit a non-thermal radio synchrotron spectrum. One such object has, however, been identified in the dwarf galaxy IC 10 (Heesen et al. 2015). The reason why it stands out against thermal and non-thermal radio emission of the host galaxy might be an unusually strong explosion, a hypernova, about 1 Myr before the time of observation. Its size is, similar to the Local Bubble,  $\sim 200$  pc. The radio spectrum is a power law with the same spectral index as the radio background,  $S(\nu) \propto \nu^{-0.6}$ . The observed non-thermal emission is 40 mJy at 1.5 GHz.

We use these properties of the non-thermal superbubble in IC 10 to estimate those of the Local Bubble as follows. First, we scale this by a factor of  $f_s = 0.1$  to account for the fact that likely none of the supernovae that shaped the Local Bubble was a hypernova. With the given spectral index, this yields a flux density of 2.7 mJy at 3 GHz. With a distance of 0.7 Mpc to IC 10, we then get a spectral luminosity of  $1.6 \times 10^{17}$  W Hz $^{-1}$ . Assuming a bubble radius of  $100f_{r10}$  pc, we obtain a volume emissivity of

$$l_\nu = 1.3 \times 10^{-39} \left( \frac{f_s}{0.1} \right) f_{r10}^{-3} \text{ W Hz}^{-1} \text{ m}^{-3} \quad (1)$$

Placing the Sun at the centre of such a non-thermal bubble yields a flux contribution from each shell at distance  $r$  of

$$dS_\nu = \frac{4\pi r^2 dr l_\nu}{4\pi r^2} = l_\nu dr. \quad (2)$$

The integral is straightforward and results, for a radius of the Local Bubble of  $100f_{rLB}$  pc in

$$S_\nu = 4 \times 10^5 \left( \frac{f_s}{0.1} \right) f_{r10}^{-3} f_{rLB} \left( \frac{\nu}{3 \text{ GHz}} \right)^{-0.6} \text{ Jy}. \quad (3)$$

The antenna temperature follows from this via  $T_\nu = S_\nu c^2 / (8\pi k_B \nu^2)$ , and so

$$T_\nu = 113 \left( \frac{f_s}{0.1} \right) f_{r10}^{-3} f_{rLB} \left( \frac{\nu}{3 \text{ GHz}} \right)^{-2.6} \text{ mK}. \quad (4)$$

This overpredicts the radio synchrotron background by a factor of 2 and thus demonstrates that the contribution of the Local Bubble can in principle be very important.

## 3 DETAILED MODEL OF THE RADIO SYNCHROTRON EMISSION OF THE LOCAL BUBBLE

Thanks to a number of measurements unique to the Local Bubble, it is possible to predict its radio emission with far better accuracy than we have done in the previous section. Both elements required to predict synchrotron emission, the energy distribution of cosmic ray electrons and positrons and the strength and geometry of the magnetic field are constrained by recent experimental data. The Alpha Magnetic Spectrometer (AMS) onboard the International Space Station (ISS) has measured the near-earth energy distribution for cosmic ray electrons with energies  $E$  between 0.5 GeV and 1.4 TeV (Aguilar et al. 2019). Constraints at lower energy and outside the volume influenced by the Solar wind have been provided by Voyager I (Cummings et al. 2016). The part of this distribution relevant for the radio background can be calculated once the magnetic field is known, and constraints are available from pulsar observations. We review the observational constraints on both, magnetic field and particle energy spectrum, in the following three subsections.

### 3.1 Magnetic field constraints

The magnetic field in the local bubble is constrained by measurements of the Faraday effect, i.e. the rotation of the plane of polarization of pulses from radio pulsars, combined with the pulse dispersion as a function of frequency. Such measurements yield magnetic field strength estimates of  $B = 0.05\text{--}0.2$  nT (Xu & Han 2019), but the measurements do not contain information whether this field strength is volume filling or restricted to a small fraction of the path through the Local Bubble. Field reversals and density inhomogeneities affect the estimate. The quantities directly measured from the pulsar measurements are dispersion measure DM and rotation measure RM. For eight pulsars at distances between 90 and 140 pc, i.e. towards the edge of the Local Bubble, Xu & Han (2019) report a mean dispersion measure of  $42 \text{ cm}^{-3} \text{ pc}$  with a standard deviation of  $20 \text{ cm}^{-3} \text{ pc}$ . This corresponds to a column of free, thermal electrons of

$$N_e = (1.3 \pm 0.6) \times 10^{24} \text{ m}^{-2}. \quad (5)$$

X-ray measurements of the hot bubble plasma suggest a thermal electron density of  $n_{e,X} = (4.68 \pm 0.47) \times 10^3 \text{ m}^{-3}$  (Snowden et al. 2014). This value is very typical for superbubbles, including X-ray bright ones, as shown in 3D numerical simulations (Krause et al. 2013a, 2014). The contribution to the free electron column in the Local Bubble from the X-ray emitting plasma, again for a radius of the Local Bubble of  $100f_{rLB}$  pc is therefore

$$N_{e,X} = (1.4 \pm 0.1) \times 10^{22} f_{rLB} \text{ m}^{-2}. \quad (6)$$

Warm clouds within the Local Bubble have sizes of several parsecs and electron densities of the order of  $n_{e,wc} = 10^5 \text{ m}^{-3}$  (e.g. Gry & Jenkins 2017; Linsky et al. 2019). Assuming a total warm cloud

path-length of  $10f_{\text{wcp}}$  pc, we obtain an estimate for the corresponding free electron column of

$$N_{e,\text{wc}} = 3 \times 10^{22} f_{\text{wcp}} \text{ m}^{-2}. \quad (7)$$

Hence, neither the hot X-ray plasma nor the warm clouds and filaments contribute significantly to the pulsar dispersion measures. As Xu & Han (2019) note, the dispersion measure is probably produced predominantly by the bubble wall, an ionized mixing layer between the superbubble interior and the cold supershell (compare also Krause et al. 2014).

The root mean square rotation measure against the aforementioned eight pulsars is  $33 \text{ rad m}^{-2}$ . For a plasma with electron density  $n_e$  and line-of-sight magnetic field  $B_{\text{los}}$ , the rotation measure may be expressed as

$$RM = 8.1 \text{ rad m}^{-2} \int_{\text{Observer}}^{\text{Source}} \left( \frac{n_e}{10^6 \text{ m}^{-3}} \right) \left( \frac{B_{\text{los}}}{\text{nT}} \right) \frac{dl}{\text{pc}}, \quad (8)$$

where  $dl$  is the path-length element.

For the warm clouds, an estimate for the magnetic field strength is available from measurements of energetic neutral atoms that are thought to originate from the solar wind, are scattered by the magnetic field near the heliospheric boundary and experience charge exchange reactions (McComas et al. 2011, 2020). For the warm clouds surrounding the heliosphere this leads to an estimate of 0.3 nT (Schwadron & McComas 2019). Pressure balance with the volume filling X-ray plasma generally suggest  $\approx 0.5 \text{ nT}$  for warm clouds in the Local Bubble (Snowden et al. 2014).

Ignoring field reversals yields an upper limit for the rotation measure for given electron density, magnetic field  $B$ , and total path-length  $l_{\text{pc}}$ . For the warm clouds we write this as

$$RM < 4 \text{ rad m}^{-2} \left( \frac{n_e}{n_{e,\text{wc}}} \right) \left( \frac{B_{\text{los}}}{0.5 \text{ nT}} \right) f_{\text{wcp}}. \quad (9)$$

This suggests a perhaps non-negligible, but certainly not dominant contribution by the warm clouds to the rotation measure. Scaling to the properties of the X-ray plasma, we write equation (9) as

$$RM < 38 \text{ rad m}^{-2} \left( \frac{n_e}{n_{e,\text{X}}} \right) \left( \frac{B_{\text{los}}}{10 \text{ nT}} \right) f_{\text{tLB}}. \quad (10)$$

Consequently, the X-ray emitting plasma in the Local Bubble may be magnetized up to a level of at least 10 nT without violating the rotation measure constraint. Since we show below that very small magnetic fields will not lead to an interesting amount of radio emission, we consider in the following only magnetic field strengths between 0.1 and 10 nT.

### 3.2 Constraints on the particle energy spectrum

When averaging over the angle between the magnetic field direction and the isotropically assumed particle directions, the characteristic frequency for synchrotron emission becomes (Longair 2011)

$$\nu_c = 794 \text{ MHz} \left( \frac{E}{\text{GeV}} \right)^2 \left( \frac{B}{\text{nT}} \right). \quad (11)$$

For magnetic field strengths within the observational limits (Section 3.1), cosmic ray electrons from 50 MeV up to about 6 GeV radiate at frequencies relevant to the radio background (20 MHz to 3 GHz). Particles at these energies are strongly affected by the solar modulation, i.e. the energy spectrum changes during the propagation from interstellar space through the magnetized Solar wind before reaching the detector near Earth. The Voyager 1 spacecraft has left the region influenced by the Solar wind in 2012 and has since then

measured electron energy distributions in the range 2.7–79 MeV in the local interstellar medium (Cummings et al. 2016). Cosmic ray propagation models constrained by Voyager 1 and AMS data (Aguilar et al. 2019) have been developed that infer the cosmic ray electron density distribution in the local interstellar medium, outside the Solar wind bubble for energies between 1 MeV and 1 TeV (Vittino et al. 2019). The resulting distribution can be approximated by  $n(E) \propto E^{-p}$ , with  $p = 1.4$  (3.1) below (above) 1 GeV. Orlando (2018) derived a very similar electron energy distribution and showed that the expected inverse Compton emission is consistent with gamma-ray observations. Positrons, which are to a large part produced by hadronic interactions (Strong, Orlando & Jaffe 2011), contribute at a level of several per cent to the all electron energy spectrum in the relevant GeV range, and are included in our model.

Turbulent mixing is expected to homogenize the electron energy spectrum throughout the Local Bubble, even though tangled magnetic fields may prevent free streaming: The gyroradius is a function of electron energy  $E$  and magnetic field  $B$  and is given by

$$r_g = 3 \times 10^{-7} \text{ pc} \left( \frac{E}{\text{GeV}} \right) \left( \frac{B}{\text{nT}} \right)^{-1}. \quad (12)$$

The cosmic ray electrons relevant to the radio background would hence have gyroradii between  $10^{-9}$  and  $10^{-5}$  pc. The particles are therefore tied to probably tangled magnetic field lines locally. Still, mixing is expected to occur due to gas sloshing caused by off-centre supernovae (Krause et al. 2014). The characteristic time-scale is the turnover time-scale of the bubble, which can be approximated by the sound crossing time (e.g. Krause et al. 2013b). We argue in Section 3.3 that the Local Bubble has evolved probably for several crossing times since the last supernova about 1.5–3.2 Myr ago. Therefore, cosmic ray electrons produced by that supernova or any source that contributed on a similar time-scale are now well mixed throughout the superbubble. In the following, we use the electron and positron energy spectra tabulated in Vittino et al. (2019) as representative for the cosmic ray electron energy spectrum in the Local Bubble.

### 3.3 Constraints on the magnetic field geometry

The geometry and intermittency of the magnetic field shapes the directional dependence of the radio synchrotron emission. Supernovae in superbubbles drive gas sloshing on the scale of the superbubble diameter, which leads to decaying turbulence (Krause et al. 2014). Deposits of radioactive  $^{60}\text{Fe}$  in deep sea sediments suggest that the last supernova in the Local Bubble occurred 1.5–3.2 Myr ago (Wallner et al. 2016). The characteristic decay time for turbulence is the sound crossing time. Using a characteristic diameter of 300 pc (Pelgrims et al. 2020) and a sound speed of  $160 \text{ km s}^{-1}$  (for an X-ray temperature of 0.1 keV, Snowden et al. 2014) gives a sound crossing time of 1.8 Myr. Superbubbles with sizes comparable to the Local Bubble may have higher temperatures shortly after the supernova explosion (Krause et al. 2018). Therefore, turbulence may have evolved effectively by several decay times since the last explosion. Additional kinetic energy may currently be injected by a nearby pulsar wind, which is required to explain the observed abundance of high-energy electrons and positrons measured by AMS (López-Coto et al. 2018; Bykov et al. 2019).

Observationally, the magnetic field geometry is constrained by starlight polarization. For stars with distances 100–500 pc, a large-scale coherent field is observed towards galactic coordinates  $l = 240^\circ - (360^\circ) - 60^\circ$ , whereas a magnetic field tangled on small scales

is observed for other longitudes (Berdyugin, Piirola & Teerikorpi 2014). The directions with coherent magnetic field structure appear correlated with the direction towards which the edge of the Local Bubble is nearest (Pelgrims et al. 2020). It appears therefore plausible that the coherent structure is a feature of the bubble wall and that the interior of the Local Bubble has a magnetic field structure characterized by decaying turbulence, with the largest magnetic filaments about 40 pc long (Piirola et al. 2020).

### 3.4 Synchrotron emission model

We therefore model the magnetic field in the Local Bubble as a random field with a vector potential drawn from a Rayleigh distribution with a Kolmogorov power spectrum following, e.g. Tribble (1991) and Murgia et al. (2004). We use magnetic field cubes with 256 cells on a side. Most quantities are well converged with this resolution. For some we obtain meaningful upper limits (compare below). The approach is well tested for the description of magnetic fields in clusters of galaxies with and without radio lobes (e.g. Guidetti et al. 2010; Huarte-Espinosa, Krause & Alexander 2011; Hardcastle 2013; Hardcastle & Krause 2014). Following the experimental data on the field's geometry, we set the 85 per cent largest modes to zero. This is a reasonable approximation for decaying turbulence in the case of initially weak magnetic fields that were amplified by a strong driving event (Brandenburg et al. 2019), e.g. the sloshing following an off-centre supernova explosion (Krause et al. 2014). The magnetic field geometry is discussed further in Section 4, below. We also show models for the uncut power spectrum and for a cut at 20 per cent for comparison. We have checked that varying this cutoff has a negligible effect on the resulting sky temperature (compare Hardcastle 2013).

We put the observer in the centre of the data cube, scale the magnetic field to values within the range allowed by observations and assume a homogeneous distribution of synchrotron-emitting leptons. We derive the density of non-thermal electrons and positrons,  $n_{e,p}$ , in the local interstellar medium at a given energy, from the tabulated fluxes  $\Phi_{e,p}$  from the model of Vittino et al. (2019). The total density of non-thermal electrons and positrons,  $n(E)$ , is then obtained by summing the individual contributions.

In each energy bin, we use the two neighbouring bins to fit a local power law:  $n(E) = \kappa E^{-q}$ . This enables us to use the synchrotron emissivity for a power-law distribution of electrons (Longair 2011)

$$J(\nu) = A \frac{\sqrt{3\pi} e^3 B}{16\pi^2 \epsilon_0 c m_e (q-1)} \kappa \left( \frac{2\pi \nu m_e^3 c^4}{3eB} \right)^{-\frac{q-1}{2}} \quad (13)$$

with

$$A = \frac{\Gamma\left(\frac{q}{4} + \frac{19}{12}\right) \Gamma\left(\frac{q}{4} - \frac{1}{12}\right) \Gamma\left(\frac{q}{4} + \frac{5}{4}\right)}{\Gamma\left(\frac{q}{4} + \frac{7}{12}\right)}. \quad (14)$$

Here,  $B$  denotes the magnetic field strength perpendicular to the line of sight,  $m_e$  and  $e$  are, respectively, electron mass and charge,  $c$  is the speed of light and  $\epsilon_0$  the vacuum permittivity. We divide the sky in a  $n_{\text{lon}} \times n_{\text{lat}}$  grid of longitudes  $l$  and latitudes  $b$  with spacings  $\Delta l$  and  $\Delta b$ . For each cone of given  $l_i$  and  $b_j$ , we first select the observing frequency  $\nu$ . In each cell, we evaluate the Lorentz factor given the local magnetic field and the chosen observing frequency. We then look up the corresponding non-thermal electron densities and fit the normalization and slope of the local power law at the corresponding energy. After cutting a small region near the centre of the box (5 per cent of the path-length) to avoid resolution effects, we find the spectral flux density by summing the weighted emissivities within a

given cone

$$S_\nu(l_i, b_j) = \sum_{\text{cells in cone}} \frac{j_\nu dV}{4\pi r^2}, \quad (15)$$

where each Cartesian cell has the same volume  $dV$  and  $r$  is its distance from the centre of the grid, which will be different for each cell. The intensity is found by dividing through surface area of the corresponding sky grid cell

$$I_\nu(l_i, b_j) = \frac{S_\nu(l_i, b_j)}{dl db \sin b}. \quad (16)$$

And, finally, we get the antenna temperature from

$$T_{i,j} = \frac{I_\nu(l_i, b_j) c^2}{2k_B \nu^2}. \quad (17)$$

We also calculate polarization information. The local contributions to the Stokes parameters are (compare Hardcastle & Krause 2014)

$$\begin{pmatrix} j_I \\ j_Q/\mu \\ j_U/\mu \end{pmatrix} \propto (B_\phi^2 + B_\theta^2)^{\frac{q+1}{4}} \begin{pmatrix} B_\phi^2 + B_\theta^2 \\ B_\phi^2 - B_\theta^2 \\ 2B_\phi B_\theta \end{pmatrix}, \quad (18)$$

where  $B_\phi$  and  $B_\theta$  are the components of the magnetic field in spherical coordinates that are perpendicular to the line of sight at a given location. The maximum polarization  $\mu$  is given by

$$\mu = \frac{\alpha + 1}{\alpha + 5/3} \quad (19)$$

with the spectral index of the radio emission  $\alpha = (q - 1)/2$ . As  $q$  is fitted to for each energy bin,  $\alpha$  depends on the observing frequency. The Stokes parameters are integrated along the line of sight to obtain  $I$ ,  $Q$ , and  $U$  for each direction of the sky grid. The fractional polarization  $f$  is then computed as

$$f = \frac{\sqrt{Q^2 + U^2}}{I}. \quad (20)$$

### 3.5 Modelling results

The sky distribution of antenna temperature is shown for parameters suitable for comparison to the ARCADE 2 experiment in the top row of Fig. 1. The polarization map for the corresponding model is shown in the bottom row of the same figure. The observing frequency is 3.3 GHz and the spatial resolution is  $12^\circ$ .

We have chosen three different cuts  $k_{\text{min}}$  in the power spectrum for the magnetic field (compare Section 3.4). The left column is for an uncut Kolmogorov power spectrum. The middle (right) one for the case where the 20 (85) per cent largest modes are cut. Large modes in the magnetic power spectrum lead to differences in antenna temperature of a factor of a few for different sky directions. Consequently, the standard deviation of the antenna temperature is almost half of the mean value. There is little difference between the sky distributions predicted for  $k_{\text{min}} = 20$  per cent and  $k_{\text{min}} = 85$  per cent. In both cases, the distribution is smooth across the sky with maximum antenna temperature ratios below two for any two sky directions and a standard deviation of less than 10 per cent of the mean.

A noteworthy polarization signal is only predicted for the full Kolmogorov power spectrum. The more the large modes are cut, the lower the polarization, again with little difference between  $k_{\text{min}} = 20$  per cent and  $k_{\text{min}} = 85$  per cent, namely 4 per cent versus 3 per cent. We note that the polarization we give for the  $k_{\text{min}} = 85$  per cent case is an upper limit as this value was not numerically converged with our largest grid of  $256^3$  cells.

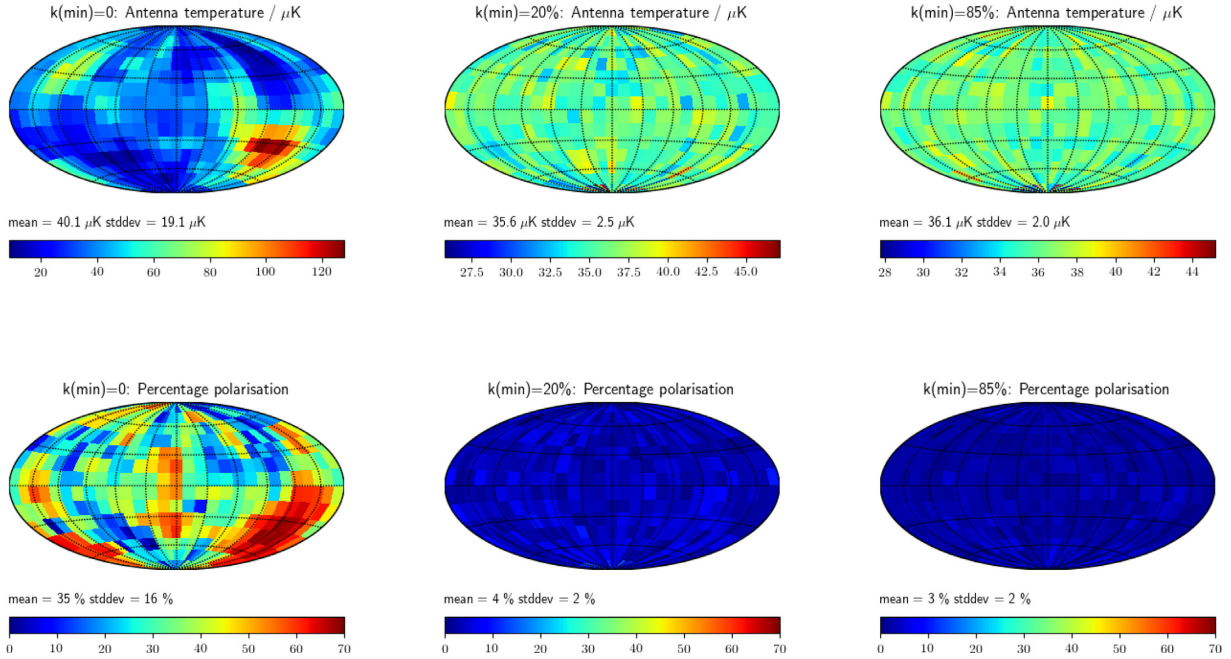


**Figure 1.** Synthetic radio sky for the detailed Local Bubble model (Section 3) with a mean magnetic field of 1.6 nT at 3.3 GHz. The resolution is  $12^\circ$  matching that of the ARCADE 2 radiometer. The top row shows the distribution of the antenna temperature. The bottom row shows the fractional polarization for the corresponding image. The left column is for a complete Kolmogorov power spectrum. The middle (right) one is for a model with the 20 (85) per cent largest modes set to zero.

We plot the mean antenna temperature against observing frequency in Fig. 2 (left). The Local Bubble has a power-law radio spectrum very similar to that of the radio background (spectral index  $\alpha \approx 0.6$ ). We compare to the measurements discussed above and reported by Seiffert et al. (2011) and Dowell & Taylor (2018). Seiffert et al. (2011) use ARCADE 2 balloon flight and lower frequency radio surveys. They subtract the Galaxy model from Kogut et al. (2011) and an estimated contribution from external galaxies from the data, and then fit a combination of the cosmic microwave background and the radio synchrotron background to the remaining spectrum. Dowell & Taylor (2018) additionally use data from the Long Wavelength Array and follow similar methods to obtain the spectrum of the radio background.

Good agreement with the data is found for magnetic field strengths between 3 and about 5 nT. For more detailed comparison to the observations, we remove the  $\nu^{-2.6}$  scaling in Fig. 2 (right). There is a slight systematic offset between the two observational data sets, which Dowell & Taylor (2018) ascribe to difficulties in the zero-level calibration of low-frequency surveys. There could also be differences due to the removal of the emission of the Galaxy. This aside, the Local Bubble model also has difficulties in simultaneously fitting the data points below and above 100 MHz. For example, for the data set by Seiffert et al. (2011), the 45 MHz data point lies on our 5 nT curve, whereas the 408 MHz data point is on our 3 nT curve.

For the reference frequency of 400 MHz, our results are well fit by the power law

$$T = 1.44 \text{ K} \left( \frac{B}{\text{nT}} \right)^{1.62}. \quad (21)$$

## 4 DISCUSSION

We used the available data on relativistic particles, magnetic fields, and thermal components to model the radio synchrotron emission of

the Local Bubble. We find that the predicted radio spectra show an approximate scaling of the antenna temperature with frequency as  $T \propto \nu^{-2.6}$ . To produce the sky temperature of the ARCADE 2 excess, we require a magnetic field in the Local Bubble of 3–5 nT. This is consistent with the pulsar rotation measures, as argued in Section 3.1, above.

There are, however, some severe difficulties with this solution. First, the cosmic ray electron spectrum is curved, and this translates to a clearly visible curvature in our predicted radio spectra (Fig. 2), but does not show up in the data. The Local Bubble would of course not be the only contributor to the radio background. In fact, Condon et al. (2012) and Hardcastle et al. (2020, submitted) both find a contribution of about 25 per cent of the emission from discrete extragalactic radio sources. Still, if most of the remaining high-frequency emission were explained by the Local Bubble, it seems that the low frequency data points would require yet another contributing source. The magnetic field required to explain 75 per cent of the radio synchrotron background [using the 408 MHz data point from Seiffert et al. (2011) as a reference value] would be 2.5 nT.

At this magnetic field strength, radiative losses are still negligible: For electrons that radiate at a frequency  $\nu_c$ , we can write the loss time-scale due to synchrotron radiation as (Ginzburg & Syrovatskii 1969)

$$t_{c,\text{sync}} = 7 \text{ Myr} \left( \frac{\nu_c}{\text{GHz}} \right)^{-1/2} \left( \frac{B}{5 \text{ nT}} \right)^{-3/2}. \quad (22)$$

The dominant radiation field for inverse Compton scattering is expected to be star light with a wavelength around  $1 \mu\text{m}$ , where the energy density is approximately  $U_{\text{rad}} = 6 \times 10^{-14} \text{ J m}^{-3}$  (Popescu et al. 2017). The inverse Compton cooling time may then be written as (Fazio 1967)

$$t_{c,\text{iC}} = 0.6 \text{ Gyr} \left( \frac{E}{\text{GeV}} \right)^{-1} \left( \frac{U_{\text{rad}}}{10^{-13} \text{ J m}^{-3}} \right)^{-1}. \quad (23)$$

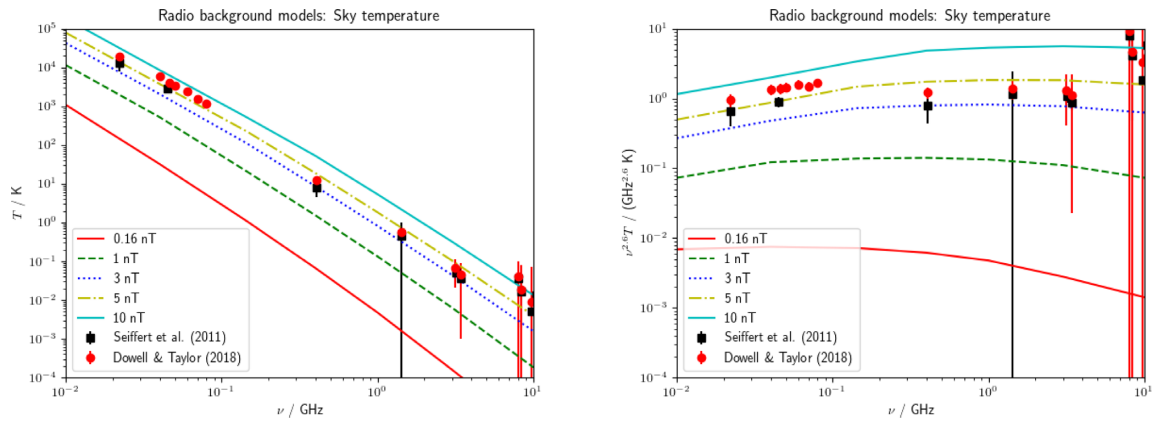


**Figure 2.** Predicted radio synchrotron emission for the Local Bubble for  $k_{\min} = 0.85$  (Section 3.5) and different mean magnetic field strengths between 0.16 nT (energy equipartition between thermal energy, cosmic ray leptonic internal energy, and magnetic energy) and 10 nT (conservative limit from Faraday rotation). Measurements are from Seiffert et al. (2011) and Dowell & Taylor (2018) as indicated in the legends. Left: antenna temperature against observing frequency. Right: Antenna temperature scaled with  $(\nu/\text{GHz})^{2.6}$ . A magnetic field strength between 3 and 5 nT is required in the Local Bubble to fully explain the radio background.

These times are long compared to the time since the last supernova, 1.5–3.2 Myr ago (compare Section 3.3), a plausible candidate for accelerating the GeV electrons (compare Sun et al. 2008). Hence, even in scenarios, where the Local Bubble explains a high fraction of the radio background, no significant curvature of the radio spectrum would be expected. Gamma-ray measurements identify a spectral break at an energy around 1 TeV (López-Coto et al. 2018). Identifying this break with the break expected from synchrotron cooling fixes the magnetic field to a value of approximately 0.2 nT.

Different magnetic field values mean that different parts of the particle spectrum are contributing to the observed emission. Therefore the curvature in the predicted spectra depends on the magnetic field strength. For magnetic field strengths around and below 1 nT, the curvature would better correspond to the one of the observed radio background. At this level of magnetic field strength, the Local Bubble would contribute about 20 per cent of the radio background between 10 MHz and 10 GHz.

The magnetic field strength for equipartition between magnetic energy and energy in relativistic leptons in our Local Bubble model is  $B_{\text{eq,rel}} = 0.16$  nT. For equipartition between magnetic and thermal energy, using the pressure of  $1.5 \times 10^{-13}$  Pa given by Snowden et al. (2014), it is  $B_{\text{eq,th}} = 0.61$  nT. A magnetic field strength of 1 nT as discussed in the previous paragraph would therefore mean an energetically dominant magnetic field. This would create tension with our assumption of the magnetic power spectrum, because, if the magnetic energy dominates, one expects an inverse cascade for the magnetic power (Christensson, Hindmarsh & Brandenburg 2001; Brandenburg, Kahnishvili & Tevzadze 2015; Reppin & Banerjee 2017; Sur 2019). The power spectrum would then be expected to be dominated by such large modes at the current time of observation. Therefore, the distributions in the left column in Fig. 1 would approximately apply, i.e. we would predict large differences of the background emission in different sky directions and significant polarization. Given that the radio background is found as an isotropic component in large sky surveys, this seems in tension with observations. A magnetic field ordered on large scales also appears to be in contradiction with the starlight polarization measurements discussed in Section 3.3, where we argued that the largest coherent scale for the magnetic field in the Local Bubble was

40 pc. We note that Singal et al. (2010) have argued against large-scale patterns in polarization for the radio background from WMAP data.

For decaying turbulence and an initially weak magnetic field, we expect magnetic field amplification up to an equilibrium with the kinetic energy (Brandenburg et al. 2019). This growth phase may last several initial crossing (turnover) times, up to perhaps ten crossing times, depending on the initial field strength. It is well known that for turbulence in general, the kinetic energy is converted to thermal energy, also on a time-scale comparable to the crossing time. The Local Bubble may therefore be in a situation close to equilibrium between magnetic and thermal energy. For this situation, we would predict a fairly isotropic contribution of about 10 per cent to the radio background.

Of course, the magnetic field might still be lower, perhaps in equipartition with the cosmic ray electrons or even lower. For a magnetic field strength of 0.16 nT, which interestingly is associated not only with equipartition between magnetic energy and relativistic leptons, but would also allow to interpret the break in the electron energy distribution at 1 TeV as due to synchrotron cooling, the Local Bubble contributes to the radio background at a level of about 1 per cent.

For a magnetic field below equipartition with the thermal energy density, we expect decaying turbulence, which would lead to a polarization of at most a few per cent with no coherent large-scale pattern in polarization (Fig. 1). This is very similar to radio polarization in the Galactic plane in general (Kogut et al. 2007).

Summarizing, a contribution of the Local Bubble to the radio background at the per cent level appears most likely.

This result is perhaps surprising, given the encouraging scalings from the non-thermal superbubble in IC 10 (Section 2). There is clearly a difference in the level of non-thermal energy and magnetic energy between the two superbubbles, and it would be interesting to understand the reasons for this better.

## 5 SUMMARY AND CONCLUSIONS

We have modelled the radio synchrotron emission of the Local Bubble, using observational constraints on the energy distribution of cosmic ray electrons, magnetic fields, X-ray gas, and warm clouds

and filaments. We find that in order to explain the radio synchrotron background remaining after subtraction of the Galaxy, the cosmic microwave background and the contribution of known extragalactic point sources we require a magnetic field of 2.5 nT. This would be allowed by constraints from Faraday rotation against nearby pulsars. However, in this case, the magnetic field would dominate energetically, and we would expect an inverse cascade, leading to large variations of the background emission in different sky direction, significant polarization with large coherence lengths for the magnetic field, and a synchrotron cooling break in the electron energy spectrum below 1 TeV, all of which are difficult to reconcile with observations. In order to avoid an inverse turbulent cascade associated with large anisotropies of the radio emission and significant polarization, the magnetic energy density should not exceed the thermal one, and to avoid an unobserved cooling break at electron energies below 1 TeV, the magnetic field should not exceed  $\approx 0.2$  nT. For this case, we predict a smooth emission with low polarization and a maximum contribution to the unexplained background at the per cent level. This leaves open the possibility that some of the radio background is produced at very high redshift, which is an important possibility for the interpretation of the EDGES absorption signal in the context of the epoch of reionization.

## ACKNOWLEDGEMENTS

We thank the anonymous referee for useful comments that helped to improve the manuscript. MJH acknowledges support from the UK Science and Technology Facilities Council (ST/R000905/1).

## DATA AVAILABILITY

The data and code underlying this article are available in the article and in its online supplementary material.

## REFERENCES

- Aguilar M. et al., 2019, *Phys. Rev. Lett.*, 122, 101101
- Alves M. I. R., Boulanger F., Ferrière K., Montier L., 2018, *A&A*, 611, L5
- Andersen K. J., Kachelriess M., Semikoz D. V., 2018, *ApJ*, 861, L19
- Andersson B. G., Potter S. B., 2006, *ApJ*, 640, L51
- Berdyugin A., Piirola V., Teerikorpi P., 2014, *A&A*, 561, A24
- Bouyahiaoui M., Kachelriess M., Semikoz D. V., 2020, *Phys. Rev. D*, 101, 123023
- Bowman J. D., Rogers A. E. E., Monsalve R. A., Mozden T. J., Mahesh N., 2018, *Nature*, 555, 67
- Brandenburg A., Kahniashvili T., Tevzadze A. e. G., 2015, *Phys. Rev. Lett.*, 114, 075001
- Brandenburg A., Kahniashvili T., Mandal S., Pol A. R., Tevzadze A. G., Vachaspati T., 2019, *Phys. Rev. Fluids*, 4, 024608
- Breitschwerdt D., de Avillez M. A., 2006, *A&A*, 452, L1
- Breitschwerdt D., Feige J., Schulreich M. M., Avillez M. A. D., Dettbarn C., Fuchs B., 2016, *Nature*, 532, 73
- Bykov A. M., Petrov A. E., Krassilchikov A. M., Levenfish K. P., Osipov S. M., Pavlov G. G., 2019, *ApJ*, 876, L8
- Christensson M., Hindmarsh M., Brandenburg A., 2001, *Phys. Rev. E*, 64, 056405
- Condon J. J. et al., 2012, *ApJ*, 758, 23
- Cox D. P., Reynolds R. J., 1987, *ARA&A*, 25, 303
- Cummings A. C. et al., 2016, *ApJ*, 831, 18
- Dowell J., Taylor G. B., 2018, *ApJ*, 858, L9
- Ewall-Wice A., Chang T.-C., Lazio T. J. W., 2020, *MNRAS*, 492, 6086
- Farhang A., van Loon J. T., Khosroshahi H. G., Javadi A., Bailey M., 2019, *Nat. Astron.*, 3, 922
- Fazio G. G., 1967, *ARA&A*, 5, 481
- Fixsen D. J. et al., 2011, *ApJ*, 734, 5
- Frisch P. C. et al., 2015, *ApJ*, 814, 112
- Galeazzi M. et al., 2014, *Nature*, 512, 171
- Ginzburg V. L., Syrovatskii S. I., 1969, *ARA&A*, 7, 375
- Gry C., Jenkins E. B., 2014, *A&A*, 567, A58
- Gry C., Jenkins E. B., 2017, *A&A*, 598, A31
- Guidetti D., Laing R. A., Murgia M., Govoni F., Gregorini L., Parma P., 2010, *A&A*, 514, A50+
- Hardcastle M. J., 2013, *MNRAS*, 433, 3364
- Hardcastle M. J., Krause M. G. H., 2014, *MNRAS*, 443, 1482
- Hardcastle M. J. et al., 2020, preprint ([arXiv:2011.08294](https://arxiv.org/abs/2011.08294))
- Heesen V. et al., 2015, *MNRAS*, 447, L1
- Hooper D., Belikov A. V., Jeltema T. E., Linden T., Profumo S., Slatyer T. R., 2012, *Phys. Rev. D*, 86, 103003
- Huarte-Espinosa M., Krause M., Alexander P., 2011, *MNRAS*, 417, 382
- Kogut A. et al., 2007, *ApJ*, 665, 355
- Kogut A. et al., 2011, *ApJ*, 734, 4
- Krause M., Fierlinger K., Diehl R., Burkert A., Voss R., Ziegler U., 2013a, *A&A*, 550, A49
- Krause M., Charbonnel C., Decressin T., Meynet G., Prantzos N., 2013b, *A&A*, 552, A121
- Krause M., Diehl R., Böhringer H., Freyberg M., Lubos D., 2014, *A&A*, 566, A94
- Krause M. G. H. et al., 2018, *A&A*, 619, A120
- Lallement R., Vergely J.-L., Valette B., Puspitarini L., Eyer L., Casagrande L., 2014, *A&A*, 561, A91
- Linsky J. L., Redfield S., Tilipman D., 2019, *ApJ*, 886, 41
- Liu B., Jaacks J., Finkelstein S. L., Bromm V., 2019, *MNRAS*, 486, 3617
- Longair M. S., 2011, *High Energy Astrophysics*. Cambridge Univ. Press, Cambridge
- López-Coto R., Parsons R. D., Hinton J. A., Giacinti G., 2018, *Phys. Rev. Lett.*, 121, 251106
- McComas D. J., Funsten H. O., Fuselier S. A., Lewis W. S., Möbius E., Schwadron N. A., 2011, *Geophys. Res. Lett.*, 38, L18101
- McComas D. J. et al., 2020, *ApJS*, 248, 26
- Monsalve R. A., Fialkov A., Bowman J. D., Rogers A. E. E., Mozden T. J., Cohen A., Barkana R., Mahesh N., 2019, *ApJ*, 875, 67
- Murgia M., Govoni F., Feretti L., Giovannini G., Dallacasa D., Fanti R., Taylor G. B., Dolag K., 2004, *A&A*, 424, 429
- Orlando E., 2018, *MNRAS*, 475, 2724
- Orlando E., Strong A., 2013, *MNRAS*, 436, 2127
- Pelgrims V., Ferrière K., Boulanger F., Lallement R., Montier L., 2020, *A&A*, 636, A17
- Piirola V. et al., 2020, *A&A*, 635, A46
- Popescu C. C., Yang R., Tuffs R. J., Natale G., Rushton M., Aharonian F., 2017, *MNRAS*, 470, 2539
- Redfield S., Linsky J. L., 2008, *ApJ*, 673, 283
- Redfield S., Linsky J. L., 2015, *ApJ*, 812, 125
- Reppin J., Banerjee R., 2017, *Phys. Rev. E*, 96, 053105
- Schulreich M., Breitschwerdt D., Feige J., Dettbarn C., 2018, *Galaxies*, 6, 26
- Schwadron N. A., McComas D. J., 2019, *ApJ*, 887, 247
- Seiffert M. et al., 2011, *ApJ*, 734, 6
- Singal J., Stawarz Ł., Lawrence A., Petrosian V., 2010, *MNRAS*, 409, 1172
- Singal J., Kogut A., Jones E., Dunlap H., 2015, *ApJ*, 799, L10
- Singal J. et al., 2018, *PASP*, 130, 036001
- Snowden S. L., 2015, *J. Phys. Conf. Ser.*, 577, 012022
- Snowden S. L. et al., 1997, *ApJ*, 485, 125
- Snowden S. L., Egger R., Finkbeiner D. P., Freyberg M. J., Plucinsky P. P., 1998, *ApJ*, 493, 715
- Snowden S. L. et al., 2014, *ApJ*, 791, L14
- Snowden S. L., Heiles C., Koutroumpa D., Kuntz K. D., Lallement R., McCammon D., Peek J. E. G., 2015a, *ApJ*, 806, 119

- Snowden S. L., Koutroumpa D., Kuntz K. D., Lallement R., Puspitarini L., 2015b, *ApJ*, 806, 120  
Stein Y. et al., 2019, *A&A*, 632, A13  
Stein Y. et al., 2020, *A&A*, 639, A111  
Strong A. W., Orlando E., Jaffe T. R., 2011, *A&A*, 534, A54  
Subrahmanyan R., Cowsik R., 2013, *ApJ*, 776, 42  
Sun X. H., Reich W., Waelkens A., Enßlin T. A., 2008, *A&A*, 477, 573  
Sur S., 2019, *MNRAS*, 488, 3439  
Tribble P. C., 1991, *MNRAS*, 250, 726  
Vittino A., Mertsch P., Gast H., Schael S., 2019, *Phys. Rev. D*, 100, 043007  
Wallner A. et al., 2016, *Nature*, 532, 69  
Xu J., Han J. L., 2019, *MNRAS*, 486, 4275

## SUPPORTING INFORMATION

Supplementary data are available at [MNRAS](#) online.

**SI\_constants.py**  
**rndmflib\_v09.py**  
**pfp\_model\_skytemp\_02.py**  
**pfp\_make\_image\_04a.py**

Please note: Oxford University Press is not responsible for the content or functionality of any supporting materials supplied by the authors. Any queries (other than missing material) should be directed to the corresponding author for the article.

This paper has been typeset from a  $\text{\TeX/L\AA\TeX}$  file prepared by the author.